Binary Colloidal Glasses: Linear Viscoelasticity and its Link to the Microscopic Structure and Dynamics

Tatjana Sentjabrskaja,[a,‡] **Alan R Jacob,**[b,‡] **Stefan U Egelhaaf,**[a] **George Petekidis,**[b] **Thomas Voigtmann**[c,d] **and Marco Laurati,**[∗a,e]

We study the relation between the microscopic structure and dynamics and the macroscopic rheological response of glass-forming colloidal suspensions, namely binary colloidal hard-sphere mixtures with large size asymmetry (1 : 5) that span a large range of mixture compositions close to the glass transition. The dynamical shear moduli are measured by oscillatory rheology and the structure and dynamics on the single-particle level by confocal microscopy. The data are compared with Brownian Dynamics simulations and predictions from mode-coupling theory based on the Percus-Yevick approximation. Experiments, simulations and theory consistently observe a strong decrease of the intermediate-frequency mechanical moduli combined with faster dynamics at intermediate mixing ratios and hence a non-monotonic dependence of these parameters but a localization of the large particles which decreases monotonically as the fraction of small particles is increased. We find that the Generalized-Stokes Einstein relation applied to the mean square displacements of the two components leads to a reasonable estimate of the shear moduli of the mixtures and hence links the rheological response to the particle dynamics which in turn reflects the microscopic structure.

1 Introduction

Dense colloidal suspensions show complex transport phenomena and nontrivial rheological properties[1,2]. If crystallization is avoided (for example due to size polydispersity), the approach to the glass transition causes an increasingly slow structural relaxation. The rheological signature of this is viscoelasticity[3]: for an increasingly large time window of the transient elastic response, the dynamical shear modulus $G(t)$ remains close to a constant value G_∞, the Maxwell plateau modulus. Only on a time scale τ that grows rapidly as one approaches the glass transition, $G(t)$ decays to zero and indicates a viscous response. In the corresponding frequency-dependent storage and loss moduli, $G'(\omega)$ and $G''(\omega)$, low-frequency viscous behavior ($G''(\omega) \propto \omega$ and $G'(\omega) \propto \omega^2$ for $\omega\tau \ll 1$) is followed by an elastic regime ($G'(\omega) > G''(\omega)$ and both nearly constant) at higher frequency.

Glass-forming binary mixtures have attracted growing interest recently[4–11]. This is because mixing effects can drastically alter the viscoelastic response of glass-forming systems. If the constituents are different enough, glasses may occur where only one component forms a solid matrix, while the other component undergoes long-range motions[4–15]. This links these binary systems to paradigmatic statistical-physics models for transport in heterogeneous media, such as the Lorentz gas[16,17]. As a consequence, an interplay arises between two distinct types of dynamical transitions[18], namely the glass transition and a dynamical localization transition of the mobile, small species. The regime where both transitions are close to each other, i.e., where the smaller species remains mobile but each component significantly alters the structure and dynamics of the other[19,20], is of special interest because it reflects situations in realistic applications, from cellular fluids[21] to complex materials for energy storage[18], much better than the idealized Lorentz-gas model. This in particular applies to the mechanical properties of such systems, which are determined both by the crowding imposed on the small particles and by the transient rigidity of the matrix[12–15].

Here we investigate the linear rheology of binary glass-forming mixtures of hard spheres. This extends our previous experimental studies on the nonlinear rheology of binary mixtures[12–15] and theoretical work on shear moduli in two-dimensional model glass formers.[22] We determine the mechanical properties upon changing the composition at fixed overall volume fraction. This reveals a change in

---

[a] *Condensed Matter Physics Laboratory, Heinrich Heine University Düsseldorf, Germany*
[b] *FORTH/IESL and Department of Materials Science and Technology, University of Crete, 71110 Heraklion, Greece*
[c] *Theory of Soft Matter, Heinrich Heine University, Düsseldorf, Germany*
[d] *Institut für Materialphysik im Weltraum, Deutsches Zentrum für Luft- und Raumfahrt (DLR), 51170 Köln, Germany*
[e] *División de Ciencias e Ingenierías, Universidad de Guanajuato, Loma del Bosque 103, 37150 León, Mexico. Email: mlaurati@fisica.ugto.mx*
‡These authors contributed equally to this work

the frequency-dependent dynamical shear moduli, the storage modulus $G'(\omega)$ and the loss modulus $G''(\omega)$, by orders of magnitude. Using confocal microscopy and Brownian Dynamics computer simulations, we relate this pronounced change in the shear moduli to the local structure and dynamics as quantified by the radial distribution function, static structure factor, distribution of Voronoi volumes and mean-squared displacement. The shear moduli are quantitatively linked to the microscopic dynamics by the Generalized Stokes-Einstein (GSE) relation. Both, experiments and simulations, are in qualitative agreement with predictions of mode-coupling theory (MCT).

2 Methods

The composition of binary hard-sphere mixtures is described by three control parameters, namely the size ratio $\delta = d_s/d_l \leq 1$ between the diameters of the small, d_s, and large particles, d_l, the total volume fraction φ, and the composition $x_s = \varphi_s/\varphi$, with the volume fraction of small spheres φ_s. Then, the total number density n of a binary sample is given by $n = 6\varphi/(\pi \bar{d}^3)$ with $\bar{d}^3 = d_l^3/(1 - x_s + x_s/\delta^3)$. Together with the thermal energy $k_B T$, this fixes the natural unit of the mechanical moduli, $n k_B T$.

2.1 Experiment

Suspensions of poly-methylmethacrylate (PMMA) particles sterically stabilized with a layer of polyhydroxystearic acid (PHS) were prepared in a mixture of cycloheptyl bromide (CHB) and cis-decalin that closely matches the density and refractive index of the colloids. In the CHB/decalin solvent mixture, the particles acquire a small charge which was screened by adding 4 mM tetrabutylammoniumchloride[23]. This system shows almost hard-sphere behaviour. The large particles were fluorescently labeled with nitrobenzoxadiazole (NBD). Binary colloidal mixtures with size ratio $\delta \approx 0.2$, fixed total volume fraction $\varphi = 0.58$ and different mixing ratios, quantified by x_s, were prepared starting from one-component suspensions. Those were obtained by diluting a sediment of large particles of mean size $d_l = 1.76 \pm 0.02\,\mu m$ (polydispersity 0.06) and small particles of mean size $d_s = 0.350 \pm 0.004\,\mu m$ (polydispersity 0.15), respectively. For the rheological measurements, samples with $\delta \approx 0.38$ were also prepared from suspensions with $d_l = 0.72 \pm 0.01\,\mu m$ (polydispersity 0.14) and $d_s = 0.27 \pm 0.01\,\mu m$ (polydispersity 0.12). The values of the diameter and polydispersity of the particles were determined from the angular dependence of the scattered intensity and the diffusion coefficient obtained by means of static and dynamic light scattering on a very dilute colloidal suspension ($\varphi \simeq 10^{-4}$), respectively.

The average polydispersity of the mixture can be obtained as $\sigma = \sqrt{[\xi_s \langle d_s^2 \rangle + (1 - \xi_s) \langle d_l^2 \rangle]/[\xi_s \langle d_s \rangle + (1 - \xi_s) \langle d_l \rangle]^2 - 1}$, with $\xi_s = N_s/N$ the number fraction of small particles, being N_s the number of small particles and N the total number of particles in a mixture. The quantity σ presents a maximum value at $x_s \approx 0.038$ for $\delta = 0.2$ and at $x_s \approx 0.13$ for $\delta = 0.38$.

To estimate the random close packing density, a sediment of the large particles with $d_l = 1.76\,\mu m$ was diluted to a volume fraction $\varphi \simeq 0.4$ and imaged by confocal microscopy. The imaged volume was partitioned into Voronoi cells and the mean size of the Voronoi volume per particle calculated. The ratio of the mean particle volume to the mean Voronoi volume was taken as an estimate of the volume fraction of the sample. This was found to be $\varphi = 0.43$ which implies a volume fraction of the sediment $\varphi_l^{(rcp)} = 0.68$. This is close to $\varphi_l^{(rcp)} = 0.65$, as predicted by simulations for the current polydispersity[24]. The small spheres were too small to be imaged (and hence also not fluorescently labeled). Thus their volume fraction was chosen to match the rheological response of the large particles. The volume fraction of the small particles was adjusted by successive dilutions until the shear moduli normalized by $n k_B T$ matched the ones of the large particles. Although their linear viscoelasticity is identical within experimental uncertainty, their volume fractions are slightly different since the samples have different polydispersities. Thus the total volume fraction φ slightly depends on the composition, i.e. x_s. Furthermore, the value of φ is known to have some uncertainty[25].

Rheology measurements were performed with an AR2000ex stress controlled rheometer (TA Instruments) using a cone and plate geometry with 20 mm diameter, 2° cone angle and 0.054 mm gap size. A solvent trap was used to minimize solvent evaporation. The temperature was set to 20 °C and controlled within ± 0.1 °C via a Peltier plate. The effects of sample loading and aging were minimized by performing standard procedures. Directly after loading, a dynamic strain sweep was performed, i.e. we applied an oscillatory shear with a frequency $\omega = 1$ rad/s and an increasing strain amplitude until the sample was shear melted. Furthermore, to start with a reproducible initial state, before each measurement, flow of the sample was induced by oscillatory shear at a strain amplitude $\gamma = 300\%$. Shear was applied for the time needed to achieve a steady-state response indicating flow, i.e. for $G'(\omega)$ and $G''(\omega)$ to become time-independent, typically 200 s. Subsequently, the linear viscoelastic moduli were measured at $0.1\% \leq \gamma \leq 0.5\%$ (depending on sample) as a function of time to monitor reformation of the structure, until the moduli reached a time-independent value, i.e. a reproducible initial state of the sample. The time needed to reach this state (between 100 s and 900 s, depending on sample) was set as the waiting time before commencing a new measurement after the large amplitude oscillatory shear

test.

Confocal microscopy experiments were performed using a VT-Eye confocal unit (Visitech International) mounted on a Nikon Ti-U inverted microscope. Stacks of slices of 512×512 pixels, corresponding to a size of the x–y plane of about $50 \times 50 \, \mu m^2$, were acquired using a $100 \times$ Nikon Plan-Apo VC oil-immersion objective and a laser with $\lambda = 488 \, nm$. Each stack was composed of 101 slices which were $0.2 \, \mu m$ apart in z-direction, leading to an imaged volume of approx. $50 \times 50 \times 20 \, \mu m^3$ per stack. Stacks were acquired at a depth of about $30 \, \mu m$ from the coverslip. The time needed to acquire one stack was approximately 3.8 s. Typically, 10 different volumes were imaged for each sample and time series of 100 stacks per volume obtained to follow the dynamics of the samples. The stacks were analyzed to extract particle coordinates and trajectories using standard routines [26]. Before each confocal microscopy experiment was performed, samples were shaken and the measurements were started after a waiting time equal to that used in the rheological measurements to start from a reproducible initial state. Possible effects of aging occurring during the measurements are assumed to be negligible.

2.2 Simulations

We performed Brownian Dynamics simulations of hard sphere binary mixtures. They are based on the Langevin equation

$$\mathbf{m} \cdot \frac{\mathrm{d}\vec{U}}{\mathrm{d}t} = \vec{F}_B + \vec{F}_H + \vec{F}_P \tag{1}$$

where $\mathbf{m}$ is the generalized mass/moment of inertia tensor, $\vec{U}$ is the particle translational/rotational velocity vector, $\vec{F}_B$ is the Brownian force, $\vec{F}_H$ is the viscous drag and $\vec{F}_P$ is the deterministic non-hydrodynamic force [27,28]. Since the mass of colloidal particles is very small and the Reynolds number is much smaller than 1, the left hand side of Eq. 1 tends to zero. The Brownian force $\vec{F}_B$ is defined by

$$\langle \vec{F}_B(t) \rangle = 0 \tag{2}$$

$$\langle \vec{F}_B(t) \vec{F}_B(t + \tau_{\mathrm{step}}) \rangle = 2 k_B T (3 \pi \eta_s d) \, \mathbf{I} \, \delta(\tau_{\mathrm{step}}) \tag{3}$$

for translational processes [29]. Here $\langle ... \rangle$ denotes an average over all fluctuations, η_s the solvent viscosity, $\mathbf{I}$ the isotropic tensor, τ_{step} is the time interval of each step and δ is the Dirac delta function. The hydrodynamic force,

$$\vec{F}_H = -3 \pi \eta_s d (\vec{U} - \langle \vec{U} \rangle) \tag{4}$$

is considered as a simplified Stokes drag for an isolated particle where $\langle \vec{U} \rangle$ is the externally imposed flow field at the particle center. The interactions between the particles are introduced through the deterministic non-hydrodynamic force vector $\vec{F}_P = \vec{F}_{HS}$ reflecting the hard sphere interaction potential [28].

In our simulations, it is implemented using a potential-free algorithm [30], which has been exhaustively used previously to simulate concentrated colloidal suspensions at rest and under shear [28,31–34]. If, after an affine (due to shear) and a random (due to Brownian motion) displacement, particles i and j, with diameters d_i and d_j respectively, have come to overlap with an interparticle separation Δs, the hard sphere force is given by

$$\vec{F}_{i(j)}^{HS} = 3 \pi \eta_s d_{i(j)} \frac{\Delta \vec{r}_{i(j)}}{\tau_{\mathrm{step}}} \tag{5}$$

where $\Delta \vec{r}_{i(j)}$ is the distance that the particle i (or j) should be moved back to avoid overlap and puts the two particles at contact and the time τ_{step} is chosen based on the motion of the small particles. Here it is

$$\Delta \vec{r}_{i(j)} = \frac{d_{j(i)}}{d_i + d_j} \left(\Delta s - \frac{d_i + d_j}{2} \right) \hat{\vec{r}} \, \mathrm{H}\left(\frac{d_i + d_j}{2} - \Delta s \right) \tag{6}$$

where the prefactor $d_{j(i)}/(d_i + d_j)$ accounts for the polydispersity, $\hat{\vec{r}}$ is the unit vector connecting the centers of the particles i and j and H is the Heaviside function. The simulation box is simultaneously divided into small and large cubic cells with the length of each cell identical to the small and large particle radius, respectively. The small particle and large particle cell lists are separately identified in each time step. Then the algorithm steps through the small and large cells in order to identify overlaps between small and large neighbors respectively. The overlaps of small and large particles are evaluated when stepping through the large cells only. The advantage of this procedure is threefold: the code efficiently identifies neighbors, avoids omitting particles during the removal of overlaps and saves computation time by avoiding repetitions in finding particle overlaps.

The total stress $\mathbf{\Sigma}$ is calculated based on the interparticle forces during each collision. Then the bulk stress is defined as total stress per unit volume [28]

$$\langle \mathbf{\Sigma} \rangle = -\langle p \rangle_f \mathbf{I} - n k_B T \, \mathbf{I} - n \langle \vec{x} \vec{F}_{HS} \rangle + 2 \eta_s \left(1 + \frac{5}{2}\varphi\right)\langle \mathbf{E} \rangle \tag{7}$$

where $\langle p \rangle_f$ is the average fluid pressure, $-n k_B T$ is the isotropic pressure due to Brownian motion, $\langle \vec{x} \vec{F}_{HS} \rangle$ represents the rheological contribution of the stress tensor and $2 \eta_s (1 + \frac{5}{2}\varphi)\langle \mathbf{E} \rangle$ is the hydrodynamic contribution to the stress that reduces to the single particle Einstein correction where $\langle \mathbf{E} \rangle$ is the rate of strain tensor. Thus the scaled dimensionless shear stress is Σ_{xy}, one of the components in the stress tensor, corresponding to the summation of all interparticle distances moved when fixing particle overlaps and collisions, i.e.

$$\Sigma_{xy} = -\frac{n}{\tau_{\mathrm{step}} N} \sum_{i=1}^{N} r_i^x \Delta r_i^y \tag{8}$$

where r_i^x is the x-component of the position and Δr_i^y is the y-component of the displacement of particle i.

The simulations were performed with size ratio $\delta = 0.2$ and volume fraction $\varphi = 0.58$ to mimic the experimental parameters. Periodic boundary conditions were used in order to avoid wall effects and reduce finite size effects. To avoid crystallization, for $x_s \geq 0.9$ the polydispersity of the small particles was chosen to be 0.10, drawn from a discrete Gaussian distribution, while the large particles were monodisperse for all compositions. For $x_s = 1$, the number of particles was $N = 15,000$, whilst $N = 50,000$ for other values of x_s. In all the above cases, the particles where initially randomly placed and allowed to equilibrate for a minimum of $100\,\tau_0$, i.e. $10^6\,\tau_{\text{step}}$, where $\tau_0 = d_i^2/D_i^0$ with $D_i^0 = k_{\text{B}}T/(3\pi\eta_s d_i)$ the free diffusion coefficient. The equilibration was considered completed once the average osmotic pressure had reached a steady state value. It was checked that this was fulfilled before microscopic structural and dynamical information was gathered and shear tests performed.

2.3 Theory

The mode-coupling theory (MCT)[35] describes the dynamics of dense liquids in terms of density correlation functions. For a mixture of N particles with species labeled by Greek indices, the basic quantity is the collective density correlator $\Phi_{\alpha\beta}(q,t) = \langle \rho_\alpha(\vec{q},t)^* \rho_\beta(\vec{q},0) \rangle$, where $\rho_\alpha(\vec{q},t) = \sum_{k=1}^{N_\alpha} \exp[i\vec{q}\cdot\vec{r}_{\alpha,k}(t)]$ are the density fluctuations to wave vector $\vec{q}$ of the $N_\alpha = \tilde{x}_\alpha N$ particles of species α. The theory assumes that the system remains homogeneous and isotropic.

In the MCT framework, one derives an approximate equation of motion for $\Phi_{\alpha\beta}(q,t)$ that embodies slow dynamics through a Mori-Zwanzig memory kernel. For overdamped colloidal dynamics without hydrodynamic interactions,

$$\tau^0(q)\partial_t\Phi(q,t) + S(q)^{-1}\Phi(q,t) \\ + \int_0^t M(q,t-t')\partial_{t'}\Phi(q,t')\,dt' = 0 \quad (9)$$

in obvious matrix notation, $\tau_{\alpha\beta}^0(q) = 1/(q^2 D_\alpha^0)\delta_{\alpha\beta}$ is a diagonal matrix of short-time diffusion coefficients and $S(q) = \Phi(q,0)$ is the matrix of partial static structure factors. The equation is closed in MCT by

$$M_{\alpha\beta}(q,t) = \frac{n}{2q^2\tilde{x}_\alpha\tilde{x}_\beta}\int\frac{d^3k}{(2\pi)^3}\sum_{\gamma\delta\lambda\mu}V_{\alpha\gamma\delta}(\vec{q},\vec{k})\Phi_{\gamma\lambda}(k,t)\times \\ \times\Phi_{\delta\mu}(p,t)V_{\beta\lambda\mu}(\vec{q},\vec{k}), \quad (10)$$

where $p = |\vec{q}-\vec{k}|$. The vertices are given in terms of the static structure functions; introducing the direct correlation function

matrices $c(q) = (X^{-1} - S^{-1}(q))/\rho$ (with $X_{\alpha\beta} = \tilde{x}_\alpha\delta_{\alpha\beta}$), we use

$$V_{\alpha\alpha'\alpha''}(\vec{q},\vec{k}) = \delta_{\alpha\alpha''}(\vec{q}\cdot\vec{k})c_{\alpha\alpha'}(k)/q \\ + \delta_{\alpha\alpha'}(\vec{q}\cdot\vec{p})c_{\alpha\alpha''}(p)/q. \quad (11)$$

Here, static triplet correlation functions have been neglected. For details, we refer to the literature[36,37].

In studying self-diffusion, also the tagged-particle density correlation function $\phi_\alpha^s(q,t) = \langle\rho_\alpha^s(\vec{q},t)^*\rho_\alpha^s(\vec{q},0)\rangle$ is of interest, where $\rho_\alpha^s(\vec{q},t) = \exp[i\vec{q}\cdot\vec{r}_\alpha^s(t)]$ is the density fluctuation of a tagged particle of species α. In the limit $q\to 0$ one obtains an expression for the mean-squared displacements (MSD), $\delta r_\alpha^2(t)$, of a particle of species α,

$$\partial_t\delta r_\alpha^2(t) + \frac{d}{dt}\int_0^t \hat{m}_\alpha^s(t-t')\partial_{t'}\delta r_\alpha^2(t')\,dt' = 6D_\alpha^0. \quad (12)$$

Here, $\hat{m}_\alpha^s(t)$ is a memory kernel derived from the one determining tagged-particle correlation functions. In particular, for liquid states its integral is finite, so that asymptotically for long times $\delta r_\alpha^2(t) \sim 6D_\alpha t$ with the long-time self-diffusion coefficient of species α

$$D_\alpha = \frac{D_\alpha^0}{1 + D_\alpha^0\int_0^\infty \hat{m}_\alpha^s(t)\,dt}. \quad (13)$$

In the ideal glass, MCT predicts the MSD to saturate, $\Delta r_\alpha^2(t) \to 6r_{\text{loc},\alpha}^2$, indicating particle localization to within a typical localization length given by $r_{\text{loc},\alpha} = 1/\sqrt{\hat{m}_\alpha^s(t\to\infty)}$.

In the MCT approximation the collective density correlation functions determine the dynamical shear modulus through the $q\to 0$ limit of the memory kernels appearing in the equation of motion,

$$G(t) = nk_{\text{B}}T\lim_{q\to 0}\sum_{\alpha\beta}\tilde{x}_\alpha M_{\alpha\beta}^{\text{T}}(q,t)\tilde{x}_\beta. \quad (14)$$

Here, $M^{\text{T}}(q,t)$ is the transverse-force memory kernel obtained by replacing in $M(q,t)$ the vector $\vec{q}$ by a vector $\vec{q}^{\text{T}}$ perpendicular to $\vec{q}$ and of equal length. In the liquid, integration of Eq. (14) over time yields the shear viscosity.

MCT describes the transition to an ideal glass state, characterized by a non-decaying contribution of the density correlation functions, called nonergodicity parameters. With $\lim_{t\to\infty}\Phi(q,t) = F(q)$, a positive definite matrix in the ideal glass, also the long-time limit of the shear modulus becomes finite, $\lim_{t\to\infty}G(t) = G_\infty$. This is the Maxwell plateau modulus. Close to the glass transition, but on the liquid side, a slow final decay from G_∞ to zero is seen whose time scale is increasing as one approaches the transition. This approach hence causes visco-elastic behavior that is typically quantified by the Fourier transformed complex shear modulus $G(\omega) = G'(\omega) + iG''(\omega)$.

Equations (9) to (12) were solved numerically using a well established scheme[36]. The time-domain equation is solved on a blockwise regular grid, with a step length that is doubled every time a new block is entered. This allows to cope with slow relaxation functions that vary on logarithmic time scales. Wave numbers are discretized according to $q_i = (i+1/2)\delta q$ with $\delta q = 0.4/d_1$ and $i = 1, \ldots 1000$. This ensures that the shear moduli in the glass, calculated from Eq. (14) as $t \rightarrow \infty$, obey the expected scaling with the particle number density when crossing over from $x_s = 0$ to $x_s = 1$. The frequency-dependent shear moduli were obtained from a Fourier transform of the time-domain solution by a simple trapezoidal method[38].

For the static structure factors needed to evaluate the MCT vertices, we resort to the Percus-Yevick (PY) approximation[39,40]. We will refer to the combination of both approximations as PY-MCT in the following. Despite its known deficiencies, the PY approximation has the advantage of being parameter-free and available in analytical form. Still, the quality of this approximation for binary mixtures and in the parameter range required by MCT, is largely unknown. Our experiments allow some test of the structure-factor input, as detailed below. Yet, the influence of approximation errors in the PY closure on MCT is difficult to estimate.

A well-known error of MCT is in the determination of the glass-transition volume fraction. For monodisperse hard spheres, PY-MCT predicts $\varphi_c \approx 0.516$ for the transition point, while experiments suggest $\varphi_c \approx 0.58$. In order to quantitatively compare the dynamic moduli and other dynamical quantities close to the transition, we thus adopt the usual procedure of using an effective shifted volume fraction in the MCT calculations. Unless noted otherwise, we will compare our experimental data at $\varphi = 0.58$ with PY-MCT results for $\varphi = 0.515$.

3 Results and Discussion

3.1 Quiescent Particle Arrangement

The structure of mixtures with different compositions is visualized through snapshots obtained from confocal microscopy and simulations (Fig.1). The successive dilution of the large particles can be appreciated in both confocal and simulation snapshots. At small values of x_s the large particles are surrounded by many other large particles. In contrast, at large x_s the small particles closely surround the large particles.

These qualitative observations can be supported by a more quantitative analysis of the structure of the mixtures, in particular using the radial distribution function

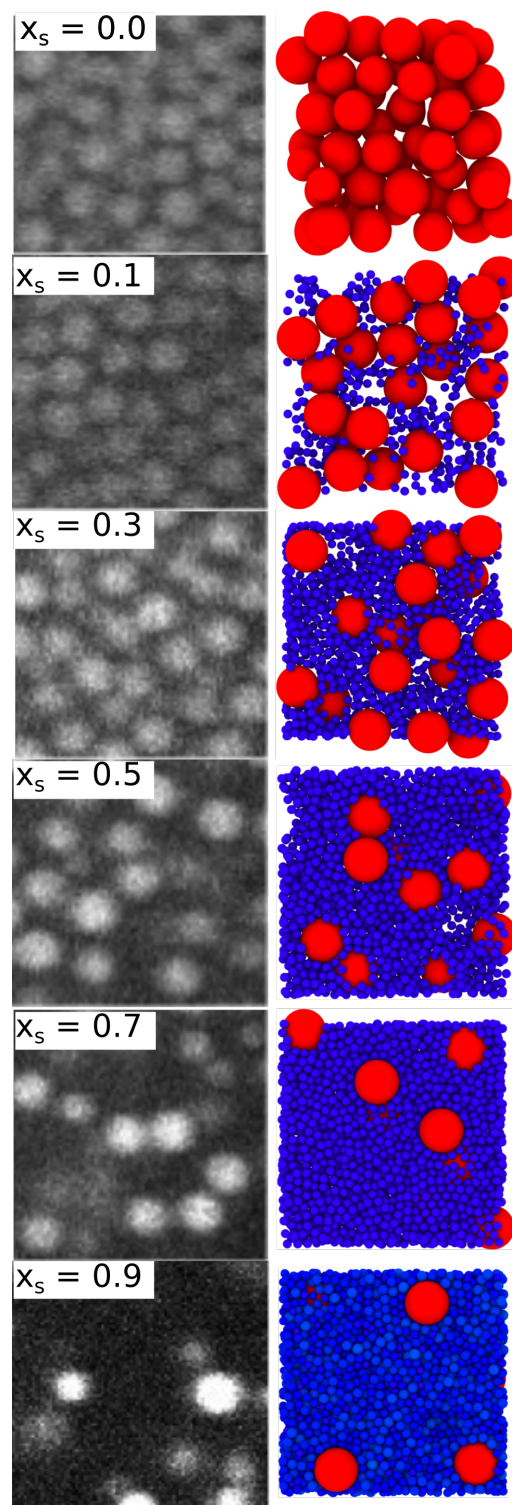$$g(r) = \frac{N(r)}{4\pi r^2 \Delta r_{sh} n} , \qquad (15)$$

Fig. 1 Confocal microscopy images (left) and simulation snapshots (right) of samples with total volume fraction $\varphi = 0.58$, size ratio $\delta = 0.2$ and different relative volume fractions of small particles, x_s, as indicated. Note that only small parts of the confocal images are shown to match the sizes of the particles in the simulation snapshots.

where $N(r)$ is the number of particles in a thin shell of thickness Δr_{sh} at distance r from a selected particle. The same information is contained in the static structure factor

$$S(q) = \Phi(q,0) = \frac{1}{N}\sum_{j=1}^{N}\sum_{k=1}^{N} e^{-i\vec{q}\cdot(\vec{r}_j-\vec{r}_k)} . \qquad (16)$$

From a set of microscopy images, we evaluate the radial distribution function of the large particles, $g_{ll}(r)$, and the corresponding static structure factor $S_{ll}(q)$, whereas the arrangement of the small particles is not accessible due to their small size (and the absence of fluorescent labelling). In contrast, in simulations $g_{ss}(r)$ and the corresponding $S_{ss}(q)$ can be determined with high accuracy, but the statistics of $g_{ll}(r)$ and $S_{ll}(q)$ are poor due to the smaller number of large particles. Experiments and simulations therefore complement each other.

The radial distribution functions of the large particles, $g_{ll}(r)$, as obtained from experiments are shown in Fig. 2a. The $g_{ll}(r)$ for $x_s = 0$ is typical of a glass-forming one-component system with size polydispersity. It shows a pronounced peak at $r \approx d_1$ corresponding to the first-neighbor shell and rapidly decaying layering. The simulation data for $x_s = 0$ are in good agreement with the experimental results. For $x_s = 0.1$, these features remain essentially unchanged. Upon increasing x_s further, the height of the first-neighbour peak decreases. As the short-range order of the large particles is destroyed, additional peaks emerge that correspond to distances $r \approx d_1 + d_s$ and $d_1 + 2d_s$; peaks for further $d_1 + m d_s$ ($m = 3, 4, \ldots$) can be identified for $x_s \geq 0.7$. As more and more large particles are replaced by small particles, it becomes more probable that large particles are separated by small particles. Moreover, for $x_s = 0.3$ one also identifies a bump at $r \approx 2d_1 + d_s$ that replaces the one at $2d_1$ for lower x_s. This layering beyond two large-particle distances disappears with increasing x_s.

The static structure factor of the large particles, $S_{ll}(q)$, reflects the progressive dilution of the large particles indicated by the decreasing height of the first peak and its shift towards smaller q (Fig. 2b). To compare $S_{ll}(q)$ from experiments and simulations with predictions of the Percus-Yevick (PY) approximation, the PY approximation is based on $\varphi = 0.55$, i.e. a volume fraction which is lower than the volume fraction of the experimental and simulated systems. This is a widely employed correction for the PY approximation[41]. The PY approximation typically overestimates the height of the structure factor peak compared to experimental data. The heights of the peaks and their positions agree, except for $x_s = 0$ where the theoretically predicted peaks are considerably larger and where a slight mismatch in the length scale of the oscillations is observed. Furthermore, at small q, where $S(q)$ is connected to the isothermal compressibility, and large $x_s = 0.7$ and 0.9, the PY approximation overestimates $S_{ll}(0)$. Nevertheless, for all x_s, the same shift in volume fraction between experiment

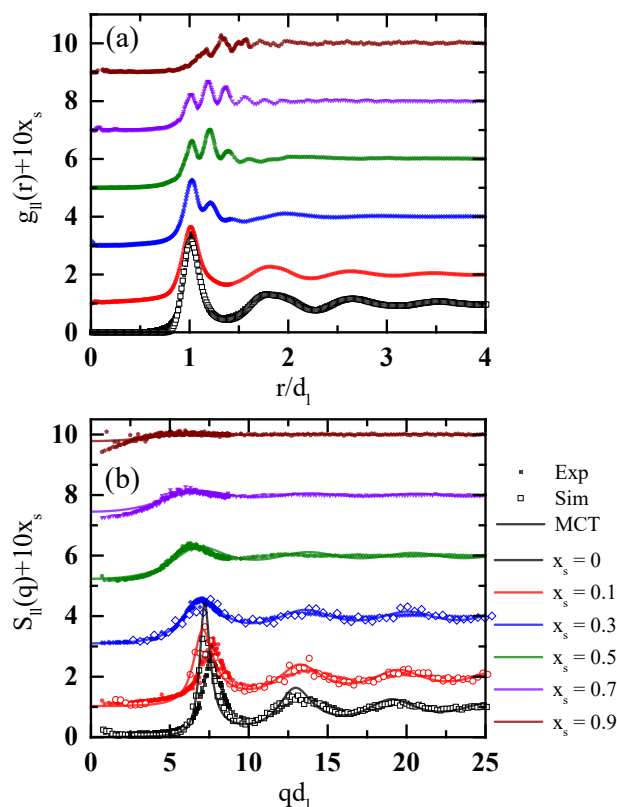**Fig. 2** (a) Radial distribution function of the large particles, $g_{ll}(r)$, obtained from confocal microscopy for total volume fraction $\varphi = 0.58$, size ratio $\delta = 0.2$ and different relative volume fractions of small particles, x_s, as indicated, shifted vertically to avoid overlap. Open circles represent simulation data for $x_s = 0$. (b) Structure factor of the large particles, $S_{ll}(q)$, as a function of dimensionless wave number qd_1 obtained from confocal microscopy for $\varphi = 0.58$, $\delta = 0.2$ and different x_s, as indicated, shifted vertically to avoid overlap. Open symbols represent simulation data for $x_s = 0$, 0.1 and 0.3. The solid lines are Percus-Yevick results for $\varphi = 0.55$.

($\varphi = 0.58$) and theory ($\varphi = 0.55$) seems to provide satisfactory agreement.

The PY approximation is also able to predict radial distribution functions. However, we do not include them in Fig. 2a for two reasons: for hard spheres polydispersity effects are much more pronounced in $g(r)$ than in $S(q)$ and, in addition, for one-component systems with $\varphi \approx 0.6$ the $g(r)$ from PY are known to violate the requirement $g(r) \geq 0$. The failure of PY to reproduce $g_{ll}(r)$ well will not affect our comparison of the dynamical and rheological behaviour as obtained by theory, simulations and experiments since we use the static structure factor as input for MCT, which is formulated entirely in
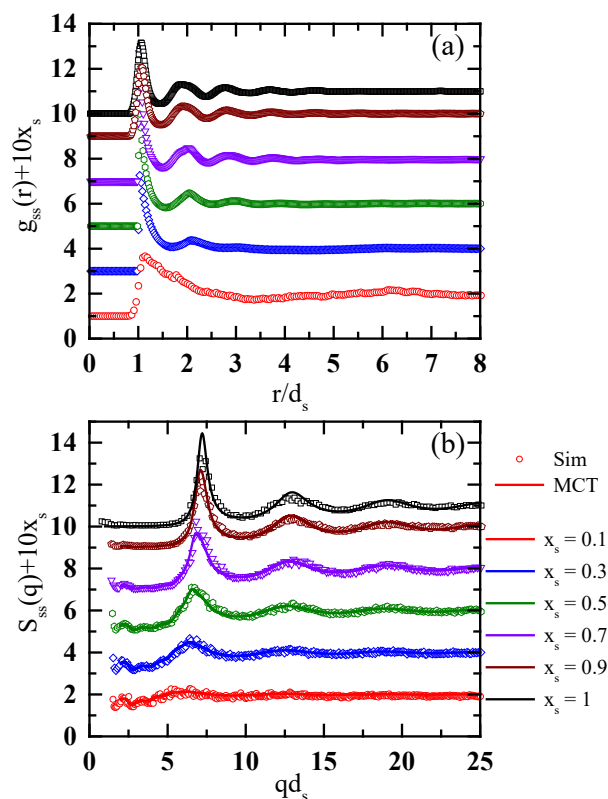
Fig. 3 (a) Radial distribution function of the small particles, $g_{ss}(r)$, obtained from simulations for total volume fraction $\varphi = 0.58$, size ratio $\delta = 0.2$ and different relative volume fractions of small particles, x_s, as indicated, shifted vertically to avoid overlap. Simulation data for $x_s = 0.9$ and 1.0 are based on small particles with a polydispersity of 0.10 to avoid crystallization. (b) Structure factor of the small particles, $S_{ss}(q)$, as a function of dimensionless wave number qd_s from simulations for $\varphi = 0.58$, $\delta = 0.2$ and different x_s, as indicated, shifted vertically to avoid overlap. The solid lines are Percus-Yevick results for $\varphi = 0.55$

.

the wave-vector domain. Thus, the observed agreement in the wave-vector domain (Fig. 2b) can form the basis for a later discussion on whether possible discrepancies between MCT and simulation as well as experimental results are due to the PY approximation or are intrinsic to MCT.

The radial distribution functions of the small particles, $g_{ss}(r)$, as obtained from simulations are shown in Fig. 3a. The evolution of the arrangement of the small particles with increasing x_s evidences the progressive crowding of the small particles, with the growth of the first peak and the appearance and also growth of higher order peaks. For most of the samples

no peculiar structural arrangements of small and large particles can be discerned. Only for $x_s = 0.1$ a large distance peak at $r/d_s \approx 6.5$ is observed, which could be associated with a configuration where two small particles are separated by one large particle. This is probably the only sample where this correlation is significant: for larger x_s the number of small spheres is so large that these configurations become irrelevant. Note that for $x_s = 0.9$ and 1.0 a polydispersity of the small spheres of 0.10 is chosen to avoid crystallization, which leads to a broader and smoother first peak.

Fig. 3b shows the small-particle static structure factors, $S_{ss}(q)$, obtained from simulations. Similar to the case of the large spheres, $g_{ss}(r)$ and $S_{ss}(q)$ show the progressive crowding of the small spheres with increasing x_s, resulting in increasingly pronounced peaks. A comparison with PY calculations with $\varphi = 0.55$ shows satisfactory agreement. Thus, it is justified to apply this approximation also to calculate the structure factors of the small particles and use them as input for MCT.

3.2 Voronoi Volume

In order to better quantify the local packing of the large and small particles as a function of mixing, we construct a Voronoi tessellation of the simulation volumes[42] which yields the Voronoi volume V_{vor} of each individual particle. The probability density functions of these volumes for the small and large particles are presented in Fig. 4.

For both species, with increasing x_s, $P(V_{vor})$ moves to smaller volumes V_{vor}, i.e. the average Voronoi volume $\langle V_{vor} \rangle$ becomes smaller and hence the local volume fraction $\varphi_{loc} = (4\pi/3)d_i^3/V_{vor}$ larger and the packing tighter (Fig. 4c). This supports our finding that, with increasing x_s, the small particles form increasingly tight cages around the large particles but also around other small particles. The particularly tight cage of small particles around large particles is also reflected in the much higher local volume fraction of the large particles as compared to the small particles.

The probability density functions of Voronoi volumes of the large particles becomes very narrow for large x_s. Interestingly, with increasing x_s the width of $P(V_{vor})$ of the small particles first becomes narrower, up to $x_s = 0.7$, and then broadens again. This suggests that around x_s the environment of small particles is most homogeneous. This is consistent with the radial distribution function $g_{ss}(r)$ which, for $x_s = 0.7$, shows a modulated second peak and the most pronounced oscillations suggesting relatively high homogeneity (Fig. 3a). Moreover, the relatively pronounced peak of $g_{ll}(r)$ at $r = d_l + d_s$ for $x_s = 0.7$ indicates a well-developed layer of small particles surrounding each large particle whereas different arrangements seem to simultaneously exist for other compositions.
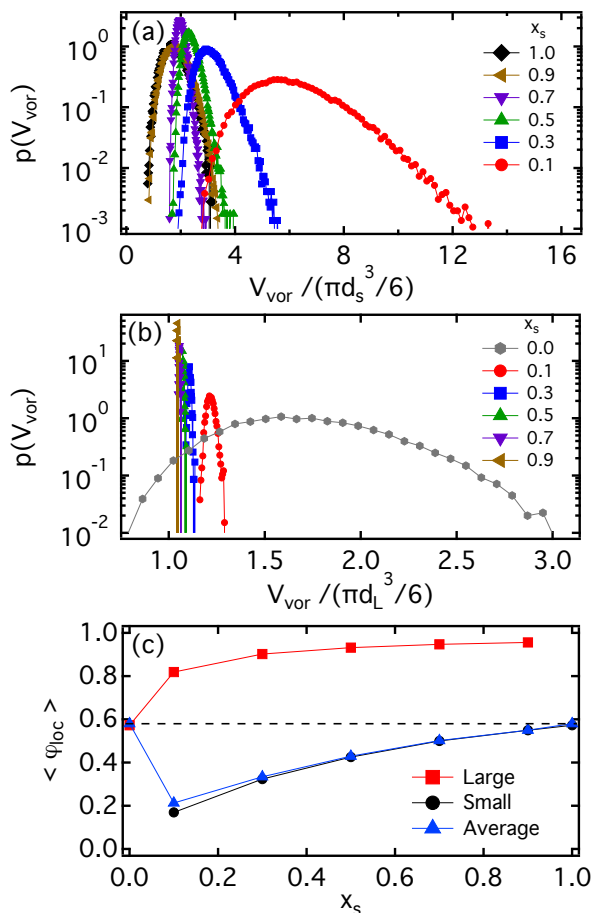
Fig. 4 Probability density function of Voronoi volumes $p(V_{vor})$ from simulations for total volume fraction $\varphi = 0.58$, size ratio $\delta = 0.2$ and different relative volume fractions of small particles, x_s, as indicated, for (a) small and (b) large particles. (c) Mean local volume fraction $\langle \varphi_{loc} \rangle$ of the small and large spheres as well as their number average as a function of the composition, i.e. x_s. The dashed line indicates the total volume fraction $\varphi = 0.58$.

3.3 Linear Viscoelasticity

We next discuss the frequency-dependent shear moduli $G'(\omega)$ and $G''(\omega)$. The results are presented in terms of a dimensionless frequency, $Pe_\omega = 3\pi\eta_s\omega\bar{d}^3/(k_BT)$, the oscillatory Péclet number. It quantifies the ratio between the timescales determined by the oscillatory perturbation, $t_\omega \sim 1/\omega$, and the average Brownian diffusion time $\langle \tau_0 \rangle$. Fig. 5 shows the x_s dependence of the storage modulus $G'(x_s)$ in units of the thermal energy per average particle volume, i.e. nk_BT, at fixed $Pe_\omega = 0.4$. The normalization ensures that the limiting cases $x_s = 0$ and $x_s = 1$, both representing one-component systems, are characterized by about the same value, $G' \approx 45nk_BT$
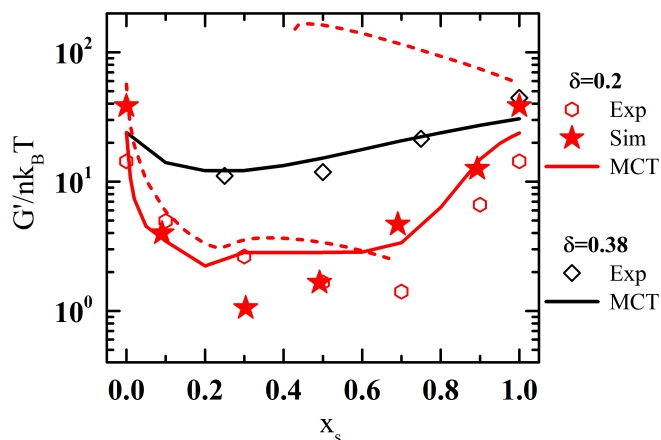

Fig. 5 Storage modulus G' as a function of the total volume fraction of small particles, x_s, for size ratios $\delta = 0.2$ and $\delta = 0.38$ (as indicated) at fixed oscillatory Péclet number $Pe_\omega = 0.4$ and total volume fraction $\varphi = 0.58$ (experiments and simulations) and $\varphi = 0.515$ (PY-MCT). Dashed lines represent the true plateau modulus G_∞ along the PY-MCT glass transition for $\delta = 0.2$ where the two branches correspond to two kinds of glasses.

in the present case, by removing a trivial increase in G' by about a factor 110 because n varies by a factor $1/\delta^3$. A pronounced minimum is seen in $G'/(nk_BT)$ as a function of x_s. For $\delta = 0.2$, it is lowered by more than one decade with the minimum around $x_s = 0.3$. Experiments and simulations show qualitative agreement. The same trend is predicted by PY-MCT, although the theory somewhat underestimates the magnitude of the decrease. It is interesting to note that the non-monotonic trend of $G'(x_s)$ can be connected to structural changes manifested in the $g_{ll}(r)$ of the large spheres; the cage of large particles is first disrupted by the intercalation of small particles and then replaced by a cage of small particles. For $\delta = 0.38$ the decrease is less pronounced, as previously reported[12], which is attributed to the reduced ability of the small particles to penetrate the cage of large particles. Experimental results and MCT predictions show a satisfactory agreement.

PY-MCT predicts the appearance of multiple glass states in the present system[10]. If the length scales associated to amorphous structures formed by the large and the small particles are sufficiently different, in a mixture of both, the transition between the glassy structures Formed at $x_s = 0$ and $x_s = 1$, respectively, is not continuous but discontinuous in the dominant length scale as manifested by a discontinuous change in the structure factor as x_s is changed. In the linear rheology, this is evidenced by a sudden change in G_∞ upon increasing φ in a glass at intermediate x_s. In Fig. 5 (dashed lines), the values
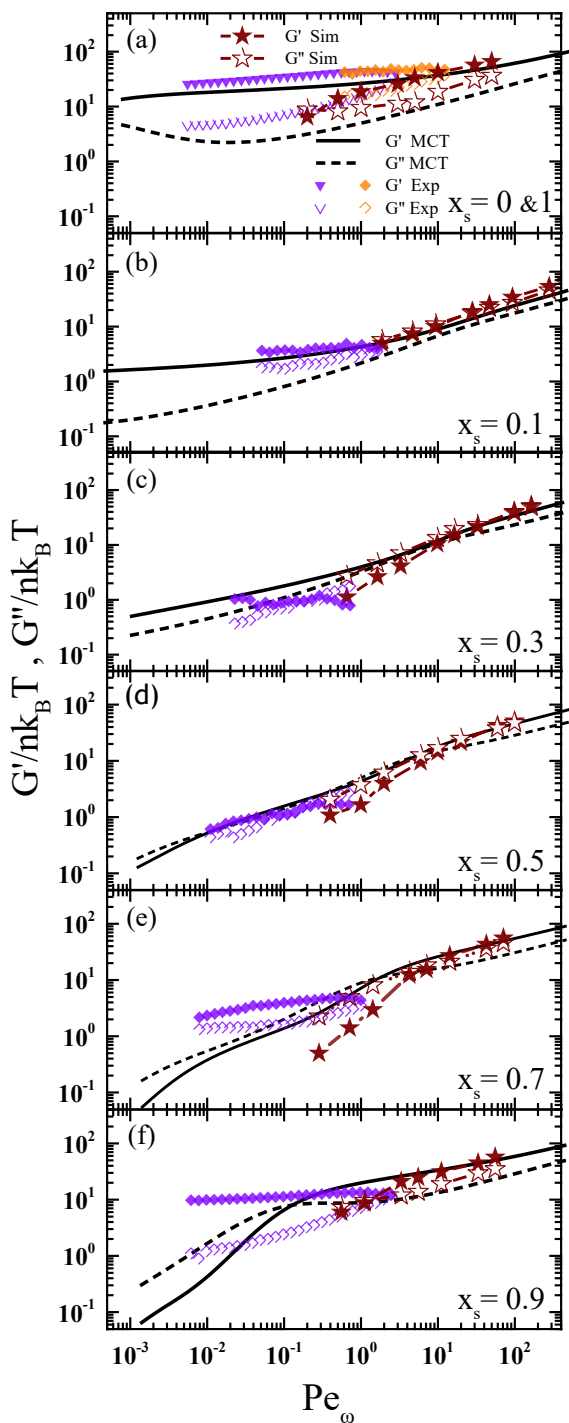
Fig. 6 Dynamical storage modulus G' and loss modulus G'' as a function of the oscillatory Péclet number Pe_ω for a total volume fraction $\varphi = 0.58$, size ratio $\delta = 0.2$ and different relative volume fractions of small particles, x_s, as indicated, as obtained from experiment (filled and open diamonds and inverted triangles) and simulations (filled and open stars). Solid and dashed lines: PY-MCT results for $\varphi = 0.515$.

of the true plateau modulus G_∞ in the idealized limit $Pe_\omega \to 0$ reflect this prediction, i.e., there are two possible values in the range $0.4 \lesssim x_s \lesssim 0.7$, one corresponding to lower packing fraction and the large-particle dominated glass (dashed line extending from $x_s = 0$), one corresponding to higher packing fraction and the small-particle dominated glass (line extending from $x_s = 1$). The repulsive glass of large particles at $x_s = 0$ softens upon addition of small particles (the value of G_∞ decreases with increasing x_s). In contrast, the glass of small particles at $x_s = 1$ instead stiffens upon addition of large particles. Whereas $G_\infty(x_s)$ shows a splitting into two branches, at finite Pe_ω PY-MCT predicts that the moduli show a continuous variation which, as discussed previously, is in agreement with experimental and simulated data.

A more complete understanding of the rheological effects of mixing can be obtained from the frequency-dependent moduli $G'(\omega)$ and $G''(\omega)$, shown in Fig. 6. Overall, the $G'(\omega)$ curves reproduce the trends discussed above in connection with Fig. 5. The experimental data for $x_s = 0$ and $x_s = 1$ agree within their uncertainty after normalization (Fig. 6a), confirming the expectation that both constituents behave as hard spheres with a corresponding volume fraction. For $x_s = 0$ and 0.1 we observe $G'(\omega) > G''(\omega)$ in the measured frequency range, i.e. a transient elastic response. For $x_s = 0.3$ and $x_s = 0.5$, $G'(\omega)$ has decreased as discussed above and the system has become softer and more fluid with $G'(\omega) \approx G''(\omega)$ in the same frequency window. Increasing x_s further, a solid-like response with $G'(\omega) > G''(\omega)$ in the measured frequency range is recovered. Note that the range of Pe_ω observed in experiments increases with x_s which is due to the larger content of small particles with their larger energy density and consequently a larger rheological signal with better statistics.

The PY-MCT and BD simulation data shown in Fig. 6 extend the experimentally accessible Pe_ω range. They agree well with the experimental data for $x_s < 0.7$, whereas for $x_s = 0.7$ and $x_s = 0.9$ agreement is less satisfactory. PY-MCT predicts the mixture to be more strongly fluidized than observed in our experiments which is in agreement with the stronger elastic response seen in experiments for larger Péclet numbers only. In contrast, agreement with simulations is more satisfactory, even though the moduli show a more pronounced fluid-like response for all values of x_s. The discrepancy between experimental, theoretical and simulation results at large x_s might be due to several reasons. Due to the different polydispersities of the two particle species (0.06 and 0.15 for the large and small particles, respectively), the effects of polydispersity might change with x_s which is neither accounted for in the theory nor in the simulations. The different polydispersities together with the adjusted equivalent rheological response (Sec. 2.1, Fig. 6a) imply slightly different volume fractions; the volume fraction of the smaller particles is expected to be larger. This might lead to a slight increase of the

volume fraction with x_s. PY-MCT predicts a strong decrease with increasing x_s[10]. Our experimental data suggest that PY-MCT overestimates this decrease, which might be related to the use of the PY approximation for $S(q)$ that becomes worse for large x_s (Fig. 2b). In addition to an x_s dependence of the volume fraction, in the experiments the absolute value of φ is known to have some uncertainty, typically at least 3 %[25], such that the actual volume fraction is expected in the interval $0.56 \lesssim \varphi \lesssim 0.60$. The simulations, which show an even more pronounced fluid-like response than PY-MCT, suggest that the experimental volume fraction might be slightly higher than assumed. Given the vicinity to the glass transition, even small variations in φ will have large effects, in particular on the dynamics.

Close to the fluid–glass transition, the loss modulus $G''(\omega)$ predicted by PY-MCT displays a broad minimum in the present frequency range. However, for $x_s \geq 0.5$ they display an S-shape of $G''(\omega)$. This shape indicates the superposition of two broad structural-relaxation peaks. This is attributed to the vicinity of two different glasses, dominated by the frozen dynamics of the small and large particles respectively, as predicted by MCT and observed experimentally[10,11]. The relaxation of glasses dominated by small and large particles at large and small Pe_ω respectively, lead to the observed S-shape of $G''(\omega)$. Furthermore, the storage modulus $G'(\omega)$ can no longer be described by an approach to a single Maxwell-type plateau but two plateau regions. These plateau regions are not very pronounced in the data since the packing fraction is significantly below the glass-transition packing fraction predicted for these x_s values. Nevertheless, the experimental and simulation data for $x_s = 0.5$ are in remarkable agreement with the broad spectrum predicted by PY-MCT. For a more detailed test of the predictions for the dynamical shear moduli, a larger frequency window and further volume fractions need to be investigated.

3.4 Quiescent Particle Dynamics

The dynamics is quantified by the mean-squared displacement (MSD)

$$\delta r_\alpha^2(t) = \langle (r_{\alpha,i}(t,t_0) - r_{\alpha,i}(0,t_0))^2 \rangle_{t_0,i} , \qquad (17)$$

where t is the delay time, t_0 a time during the particle trajectory, $\langle ... \rangle_{t_0,i}$ indicates an average over all times t_0 and all particles i and $\alpha = s, l$ refers to the small and large particles, respectively. Fig. 7 shows results obtained from experiments, simulations and theory. In general the data show the typical signature of slow structural relaxation, that is a cross-over from short-time diffusion to a broad time window with a sublinear increase before diffusion is reestablished at long times. The sublinear increase indicates subdiffusive dynamics. It is due to caging of particles by either large or small particles

which leads to a transient particle localization on a characteristic length scale.

We first discuss the experimental and simulation results for the large particles (Fig. 7a). Both data sets show similar qualitative trends. The short-time dynamics monotonically decreases with increasing x_s. In contrast, the localization length and the reestablished diffusive dynamics at intermediate and long times, respectively, are observed to first increase and then decrease with the particles being most mobile for $x_s \approx 0.3$. This is attributed to the caging transition during which a looser cage of large particles first is destroyed by the intercalation of small particles leading to a very loose first shell of neighbours at intermediate x_s. Then a successively tighter cage of small particles is formed with the small particles packing very closely around the large particles (Fig. 3). This sequence is consistent with the trend of the Voronoi volume with increasing x_s (Fig. 4). The slowdown is more pronounced in the experimental data with well-developed plateaus, while the simulations extend to the long-time diffusive regimes. This discrepancy, again, might be due to slightly different volume fractions, polydispersities and/or their dependencies on x_s and as such this is consistent with our findings for the linear viscoelasticity (see discussion in Sec. 3.3).

Fig. 7b presents a comparison between PY-MCT and simulation data, while the comparison with experiments is indirect through Fig. 7a. The experiments and simulations were performed with a volume fraction $\varphi = 0.58$, whereas the PY-MCT calculations are based on a volume fraction $\varphi = 0.515$, in order to compare states that are similarly close to the glass transitions. Using the PY structure factor, MCT is known to overestimate the tendency to glass formation in one-component hard-sphere systems and predicts a glass transition at $\varphi \approx 0.516$[35]. Thus for the PY-MCT calculations we use a lower volume fraction, $\varphi = 0.515$, and assume the shift in volume fraction between theory and experiment to be independent of x_s. With this shift in φ, PY-MCT captures the decrease of the localization length of the large particles with increasing x_s (Fig. 7b). But for long times the agreement of PY-MCT with the experimental and simulation results is poor. In contrast to the experiments, PY-MCT predicts diffusive dynamics at large x_s. Compared to simulations, the dynamics are significantly slower. This has already been reported for one-component systems[43]; close to the glass transition, MCT is known[44] to predict a much slower growth of the MSD than found in simulations, even after adjusting the packing fraction. At long times, furthermore, the trend with increasing x_s is not reproduced by PY-MCT. Comparing with previous MCT results[10], one might expect that at higher total volume fractions a better agreement for the *trend* of the long-time dynamics could be obtained. However, this would imply that the one-component dispersions of large and small particles are considerably deeper in the glass compared to the simulations and
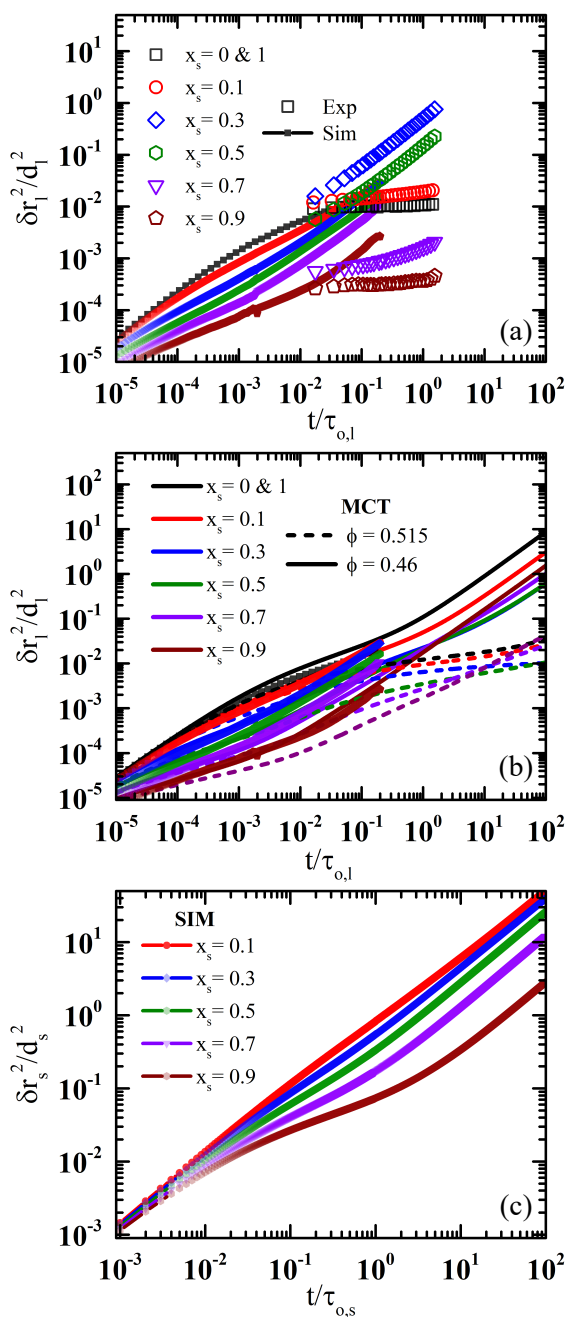
Fig. 7 Mean-squared displacement (MSD), $\delta r_\alpha^2(t)$, as a function of delay time t for size ratio $\delta = 0.2$ and different relative volume fractions of small particles, x_s, as indicated, for (a) large particles as obtained from experiments and simulations, (b) large particles as obtained from simulations (same data as in (a)) and PY-MCT, (c) small particles as obtained from simulations. The experiments and simulations were performed at a total volume fraction $\varphi = 0.58$, whereas PY-MCT results are shown for two different total volume fractions, $\varphi = 0.515$ and 0.46 (dotted and solid lines, respectively). The MSD $\delta r_\alpha^2(t)$ is normalized by the corresponding particle diameter d_α and the time t by the Brownian time of the corresponding particle in a dilute suspension, $\tau_{0,\alpha}$.

experiments. Thus, simulations and experiments do not suggest to use a higher total volume fraction for the PY-MCT. In contrast, if the total volume fraction is reduced to $\varphi = 0.46$, PY-MCT better captures the magnitude of the MSD obtained by simulations (Fig. 7b). However, as expected, the trend of the diffusivity with x_s does not agree with the simulation and experimental results. This decrease in φ accounts for a well-known issue of MCT in treating the relaxation dynamics of a tagged particle at small q, where the relaxation times are over-estimated[43].

The small particle dynamics obtained from simulations (Fig. 7c) show diffusive behavior at long times for all compositions with the long-time diffusion coefficient decreasing and the inflection point at intermediate times becoming more pronounced with increasing x_s. Both are consistent with a progressive tightening of the cage of small particles as indicated in the structural evolution represented by $g(r)$ and $S(q)$ (Fig. 3), as well as the decrease of the Voronoi volume (Fig. 4).

In the simulations and MCT calculations, solvent-mediated hydrodynamic interactions (HI) are neglected. Close to the glass transition the influence of HI on the long-time dynamics is unclear, whereas it is known to slow down the short-time diffusion. This has been shown for various size ratios and compositions, based on resummation techniques for the hydrodynamic scattering series and on Stokesian-dynamics simulations[45–47]. They suggest that the dynamics in a one-component suspension with a volume fraction comparable to ours is slowed down by a factor of 5 to 10, and slightly less in binary mixtures (cf. Fig. 3 of Ref.[46]). Thus HI could affect the Brownian time τ_0 and hence lead to a shift of the time axis in Fig. 7.

3.5 Shear Moduli Obtained through the Generalised Stokes-Einstein Relation

The shear moduli reported in Fig. 6 represent an average rheological response of the mixture and do not provide information about the contributions of the small and large particles, respectively. In contrast, the MSDs of the small and large particles have been determined individually by simulations. The Generalised Stokes-Einstein (GSE) relation provides an approximate way to link the viscoelastic moduli to the MSD[48]:

$$G^*(\omega) = \frac{2k_B T}{\pi i \omega d \mathscr{F}\{\langle \Delta r^2(t) \rangle\}} \quad (18)$$

where $\mathscr{F}\{...\}$ indicates a Fourier transform. For the one-component suspensions ($x_s = 0$ and 1), the moduli calculated using the GSE relation agree with the macroscopic moduli (Fig. 8a). This is expected as the GSE relation has been well established for one-component suspensions. However, here it needs to be extended to mixtures. Based on the MSDs of the large and small particles, the corresponding moduli
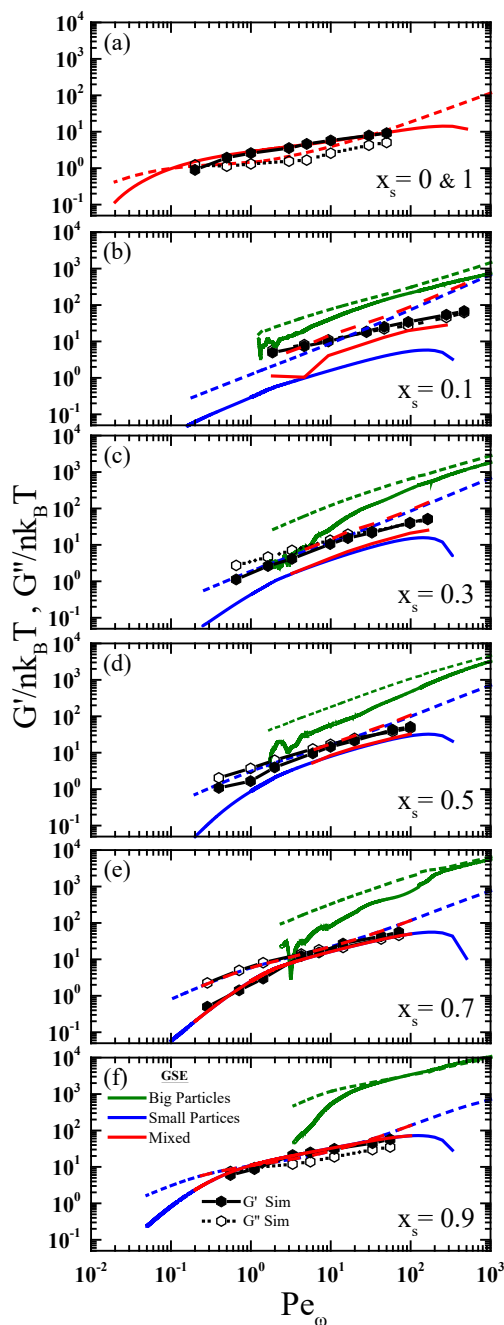
Fig. 8 Dynamical storage modulus G' and loss modulus G'' as a function of oscillatory Péclet number Pe_ω for a total volume fraction $\varphi = 0.58$, size ratio $\delta = 0.2$ and different relative volume fractions of small particles, x_s, as indicated, as obtained from simulations. Filled (open) hexagons represent the 'macroscopic' G' (G'') of the mixture (same data as in Fig. 6), solid lines the G' and dashed lines the G'' of: (blue) the small particles, (green) the large particles, all obtained through the Generalized Stokes-Einstein relation, and (red) their number-average $G'(\omega) = (n_s/(n_s+n_l))G'_s(\omega) + (n_l/(n_s+n_l))G'_l(\omega)$ (and similar for $G''(\omega)$).

of the large, $G'_l(\omega)$ and $G''_l(\omega)$, and small particles, $G'_s(\omega)$ and $G''_s(\omega)$, are calculated for each composition x_s. Based on these moduli, the number-averaged moduli are determined according to $G'(\omega) = (n_s/(n_s+n_l))G'_s(\omega) + (n_l/(n_s+n_l))G'_l(\omega)$ and similar for $G''(\omega)$ (Fig. 8). This procedure yields reasonable agreement between the directly determined 'macroscopic' moduli and the moduli calculated via the GSE relation from the microscopic dynamics.

Note that even for $x_s = 0.1$, the number fraction of small particles is huge, $n_s/(n_s+n_l) > 0.93$. Nevertheless, due to the much larger moduli of the large particles, $G'_l(\omega) \gg G'_s(\omega)$ and $G''_l(\omega) \gg G''_s(\omega)$, the large particles' contribution to the moduli is noticeable for $x_s < 0.3$. Beyond this composition, however, the number fraction of the large particles becomes so minute that the response is dominated by the small particles and the number-averaged moduli approach those obtained for the small particles. Although the range $0.1 \leq x_s \leq 0.9$ implies that we only examined suspensions with a large number fraction of small particles, the agreement indicates that the proposed procedure is appropriate. Hence the macroscopic moduli of mixtures can be estimated by the number average of the moduli of the individual species that can be obtained through the GSE relation and hence are based on the microscopic dynamics.

3.6 Osmotic Pressure

The osmotic pressure is obtained as the average of the diagonal terms of the stress tensor. Fig. 9 reports simulation results for the osmotic pressure of the mixtures as a function of x_s. It shows a non-monotonic trend with a minimum at $x_s = 0.1$. This trend resembles that of the number-averaged local volume fraction $\langle \varphi_{loc} \rangle$ (Fig. 4c). Thus, based on the Voronoi volume, the partial osmotic pressures of the small and large particles were calculated using the Carnahan-Starling equation[49] $\Pi_\alpha/n_\alpha k_B T = (1 + \langle \varphi_{loc,\alpha} \rangle + \langle \varphi_{loc,\alpha} \rangle^2 - \langle \varphi_{loc,\alpha} \rangle^3)/(1 - \langle \varphi_{loc,\alpha} \rangle)^3$, with $\alpha = s, l$ and n_α as well as $\langle \varphi_{loc,\alpha} \rangle$ depending on x_s. Neither the number nor the volume average of the partial osmotic pressures of the two species is equivalent to the total osmotic pressure obtained from the simulations. This indicates the presence of collective effects, i.e. the non-ideal mixing of the two species. If non-ideal mixing effects are taken into account[50], indeed the total osmotic pressure Π is in almost quantitative agreement with the simulation results (Fig. 9).

The non-monotonic trend of the total osmotic pressure Π as a function of x_s is similar to the dependence of the storage modulus G' (Fig. 5). Both trends can be related to the caging transition manifested in the $g_{ll}(r)$ of the large particles, in which the cage of large particles is first disrupted by the intercalation of small particles and then replaced by a cage of small particles.
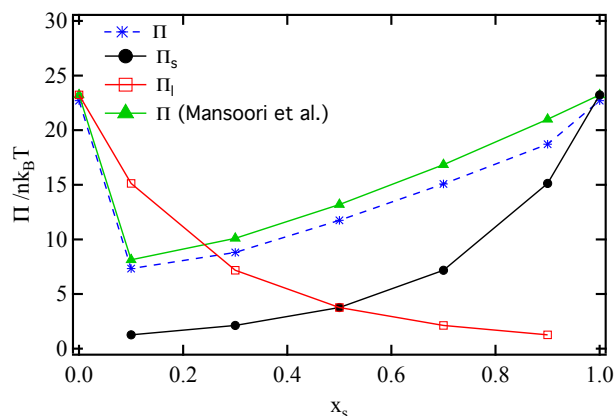
Fig. 9 Total osmotic pressure $\Pi/nk_{\mathrm{B}}T$ as a function of the relative volume fraction of small particles, x_{s}, for total volume fraction $\varphi = 0.58$ and size ratio $\delta = 0.2$ as directly obtained from simulations and calculated according to Ref. [50] based on the Voronoi volumes. The partial osmotic pressures of the small, Π_{s}, and large particles, Π_{l}, are also shown .

4 Conclusions

We performed confocal microscopy and rheology experiments as well as BD simulations and MCT calculations on binary mixtures of quasi-hard spheres. Whereas the total volume fraction $\varphi = 0.58$ and size ratio $\delta = 0.2$ were kept constant, the relative volume fraction of small particles, x_{s}, was varied. The effect of the fraction of small particles on the linear rheological response as well as the structure and dynamics on the individual-particle level was determined. Upon increasing the fraction of small particles from $x_{\mathrm{s}} = 0.0$ to about 0.5, we observe an intercalation of small particles into the cages of large particles which disrupts the cages and also reduces the mean size of the cages. This leads to changes in the dynamics, namely an increase of the long-time diffusivity of the large particles. And it also affects the rheological response which shows a softening of the glass, if probed at fixed reduced frequency. Further increasing x_{s} towards unity, the caging by small particles becomes tighter. The long-time diffusivity starts to decrease again. Correspondingly, the system again becomes less fluid and the reduced shear modulus returns to its one-component value. Therefore, changing x_{s} from 0 to 1, we observe a transition in the caging mechanism, from caging by large particles to a softening of the cage and a subsequent caging by small particles, which results in the long-time diffusivity and the reduced shear modulus both displaying a non-monotonic behaviour as a function of x_{s} with a pronounced minimum. On the other hand, the progressive trapping by the small rather than the large particles results in a monotonic decrease of the localization length of the large

particles observed at intermediate delay times.

These trends are consistently observed in the experiments, simulations and PY-MCT. However, we could not achieve a quantitative agreement in all aspects. In both, the dynamics and the shear moduli, we observe a more pronounced glassy behavior in the experiments, which might be caused by a mismatch of the total volume fractions, namely a slightly higher volume fraction in the experiments. Different polydispersities as well as x_{s} dependences of the polydispersity and total volume fraction might also play a role. Furthermore, an overestimated change in the glass transition point with x_{s} and the neglected hydrodynamic interactions in the simulations and MCT might contribute to the discrepancies.

We quantitatively linked the shear moduli to the single-particle dynamics using the Generalized Stokes-Einstein relation. The simulation results suggest that, despite the non-equilibrium conditions, the number average of the moduli of the two components, as obtained through the GSE relation, represents the macroscopic moduli. Thus, a direct link between the dynamics on an individual-particle level and the macroscopic bulk shear moduli exists. In addition, this link provides a measure to estimate the contributions of the two species to the rheological response. Similarly, the total osmotic pressure of the mixtures has been linked to the contributions of the two components with their partial osmotic pressures determined from their Voronoi volumes.

References

1 J. Mewis and N. J. Wagner, *Colloidal Suspension Rheology*, Cambridge University Press, Cambridge, 2012.
2 Th.. Voigtmann, *Curr. Opin. Colloid Interf. Sci.*, 2014, **19**, 549–560.
3 R. Larson, *The Structure and Rheology of Complex Fluids*, OUP USA, 1999.

4 A. Imhof and J. K. G. Dhont, *Phys. Rev. Lett.*, 1995, **75**, 1662–1665.

5 A. J. Moreno and J. Colmenero, *Phys. Rev. E*, 2006, **74**, 021409.

6 A. J. Moreno and J. Colmenero, *J. Chem. Phys.*, 2006, **125**, 164507.

7 E. Zaccarelli, C. Mayer, A. Asteriadi, C. N. Likos, F. Sciortino, J. Roovers, H. Iatrou, N. Hadjichristidis, P. Tartaglia, H. Löwen and D. Vlassopoulos, *Phys. Rev. Lett.*, 2005, **95**, 268301.

8 C. Mayer, E. Zaccarelli, E. Stiakakis, C. N. Likos, F. Sciortino, A. Munam, M. Gauthier, N. Hadjichristidis, H. Iatrou, P. Tartaglia, H. Löwen and D. Vlassopoulos, *Nat. Mat.*, 2008, **7**, 780–784.

9 R. Juárez-Madlonado and M. Medina-Noyola, *Phys. Rev. E*, 2008, **77**, 051503.

10 Th. Voigtmann, *Europhys. Lett.*, 2011, **96**, 36006.

11 J. Hendricks, R. Capellmann, A. B. Schofield, S. U. Egelhaaf and M. Laurati, *Phys. Rev. E*, 2015, **91**, 032308.

12 T. Sentjabrskaja, E. Babaliari, J. Hendricks, M. Laurati, G. Petekidis and S. U. Egelhaaf, *Soft Matter*, 2013, **9**, 4524–4533.

13 T. Sentjabrskaja, M. Hermes, W. C. K. Poon, C. D. Estrada, R. Castañeda-Priego, S. U. .Egelhaaf and M. Laurati, *Soft Matter*, 2014, **10**, 6546–6555.

14 T. Sentjabrskaja, M. Laurati and S. U. Egelhaaf, *Europ. Phys. J Spec. Topics*, 2017, **226**, 3023–3037.

15 T. Sentjabrskaja, J. Hendricks, A. R. Jacob, G. Petekidis, S. U. Egelhaaf and M. Laurati, *J. Rheol.*, 2018, **62**, 149–159.

16 F. Höfling, T. Franosch and E. Frey, *Phys. Rev. Lett.*, 2006, **96**, 165901.

17 F. Höfling and T. Franosch, *Phys. Rev. Lett.*, 2007, **98**, 140601.

18 Th. Voigtmann and J. Horbach, *Phys. Rev. Lett.*, 2009, **103**, 205901.

19 T. Sentjabrskaja, E. Zaccarelli, C. De Michele, F. Sciortino, P. Tartaglia, Th. Voigtmann, S. U. Egelhaaf and M. Laurati, *Nature Commun.*, 2016, **7**, 11133.

20 M. Laurati, T. Sentjabrskaja, J. Ruiz-Franco, S. U. Egelhaaf and E. Zaccarelli, *Phys. Chem. Chem. Phys.*, 2018, **20**, 18630–18638.

21 F. Höfling and T. Franosch, *Reports on Progress in Physics*, 2013, **76**, 046602.

22 R. Seyboldt, D. Hajnal, F. Weysser and M. Fuchs, *Soft Matter*, 2012, **8**, 4132–4140.

23 A. Yethiraj and A. V. Blaaderen, *Nature*, 2003, **421**, 513–517.

24 W. Schaertl and H. Silescu, *J. Stat. Phys.*, 1994, **77**, 1007–1025.

25 W. C. K. Poon, E. R. Weeks and C. P. Royall, *Soft Matter*, 2012, **8**, 21–30.

26 J. C. Crocker and D. G. Grier, *J. Coll. Interf. Sci.*, 1996, **179**, 298–310.

27 W. Russel, D. Saville and W. Schowalter, *Colloidal Dispersions*, Cambridge University Press, 1989.

28 D. R. Foss and J. F. Brady, *Journal of Rheology*, 2000, **44**, 629–651.

29 R. Kubo, *Reports on Progress in Physics*, 1966, **29**, 255.

30 D. Heyes and J. Melrose, *Journal of Non-Newtonian Fluid Mechanics*, 1993, **46**, 1 – 28.

31 N. Koumakis, M. Laurati, S. U. Egelhaaf, J. F. Brady and G. Petekidis, *Phys. Rev. Lett.*, 2012, **108**, 098303.

32 N. Koumakis, J. F. Brady and G. Petekidis, *Phys. Rev. Lett.*, 2013, **110**, 178301.

33 A. R. Jacob, A. S. Poulos, S. Kim, J. Vermant and G. Petekidis, *Phys. Rev. Lett.*, 2015, **115**, 218301.

34 N. Koumakis, M. Laurati, A. R. Jacob, K. J. Mutch, A. Abdellali, A. B. Schofield, S. U. Egelhaaf, J. F. Brady and G. Petekidis, *J. Rheol.*, 2016, **60**, 603–623.

35 W. Götze, *Complex Dynamics of Glass Forming Liquids: A Mode-Coupling Theory Approach*, Oxford University Press, Oxford, 2009.

36 W. Götze and Th. Voigtmann, *Phys. Rev. E*, 2003, **67**, 021502.

37 W. Götze, in *Amorphous and Liquid Materials*, ed. E. Lüscher, G. Fritsch and G. Jacucci, Nijhoff, Dordrecht, 1987, pp. 34–81.

38 E. O. Tuck, *Math. Comput.*, 1967, **21**, 239–241.

39 J. L. Lebowitz and J. S. Rowlinson, *J. Chem. Phys.*, 1964, **41**, 133–138.

40 R. J. Baxter, *J. Chem. Phys.*, 1970, **52**, 4559–4562.

41 J.-P. Hansen and I. R. McDonald, *Theory of Simple Liquids*, Academic Press, London, 3rd edn., 2006.

42 C. H. Rycroft, *Chaos*, 2009, **19**, 041111.

43 F. Weysser, A. M. Puertas, M. Fuchs and Th. Voigtmann, *Phys. Rev. E*, 2010, **82**, 011504.

44 T. Voigtmann, A. M. Puertas and M. Fuchs, *Phys. Rev. E*, 2004, **70**, 061506.

45 H. Zhang and G. Nägele, *J. Chem. Phys.*, 2002, **117**, 5908–5920.

46 M. Wang and J. F. Brady, *J. Chem. Phys.*, 2015, **142**, 094901.

47 M. Wang and J. F. Brady, *J. Chem. Phys.*, 2015, **142**, 064905.

48 T. G. Mason, K. Ganesan, J. H. van Zanten, D. Wirtz and S. C. Kuo, *Phys. Rev. Lett.*, 1997, **79**, 3282–3285.

49 N. F. Carnahan and K. E. Starling, *J. Chem. Phys.*, 1969, **53**, 635.

50 G. A. Mansoori, N. F. Carnahan, K. E. Starling and T. W. Leland, *J. Chem. Phys.*, 1971, **54**, 1523.